Journal of Alloys and Compounds 976 (2024) 173202

Contents lists available at ScienceDirect

Journal of Alloys and Compounds

journal homepage: www.elsevier.com/locate/jalcom

Research Article

Solution-based 3D printed thermoelectric composite for custom-shaped thermoelectric generator applications

Mingxin Bian [a], Zhiheng Xu [a,b,*], Xiaobin Tang [a,b,*], Hongyang Jia [a], Yuqiao Wang [c], Andreu Cabot [d,e]

[a] Department of Nuclear Science and Technology, Nanjing University of Aeronautics and Astronautics, Nanjing 211106, China
[b] Key Laboratory of Nuclear Technology Application and Radiation Protection in Astronautics, Ministry of Industry and Information Technology, Nanjing 211106, China
[c] Research Center for Nano Photoelectrochemistry and Devices, School of Chemistry and Chemical Engineering, Southeast University, Nanjing 211189, China
[d] Catalonia Institute for Energy Research-IREC, Sant Adrià de Besòs, Barcelona 08930, Spain
[e] ICREA, ICREA Pg. Lluis Companys, Barcelona 08010, Spain

ARTICLE INFO

Keywords:
3D printing
Conductive additive
Printability
Radioisotope thermoelectric generator
Bismuth telluride

ABSTRACT

To fulfill the ever-increasing power demands of deep space exploration, the output performance of radioisotope thermoelectric generators, the only accessible power source, must be enhanced in several aspects, including thermoelectric properties of materials, geometry, welding, etc. In this study, we present our results on the development of a novel thermoelectric slurry suitable for the 3D printing of thermoelectric generators with optimized leg geometry. The rheological properties of the slurry are optimized by combining proper amounts of organic solvent, binder, and bismuth telluride-based thermoelectric powder. The addition of Cu to the slurry as a conductive additive are also investigated. The homogeneous dispersion of Cu within the material not only increases the electrical conductivity of the final thermoelectric leg significantly but also promotes the crystallization of the thermoelectric particles during the sintering process. These effects result in 3D-printed thermoelectric composites exhibiting ZT values up to 0.91 and extended optimum operating temperature range. Thermoelectric modules composed of 3D-printed thermoelectric legs show excellent output performance and structural strength. This work could also produce other special shaped thermoelectric devices to match irregularly shaped heat sources to reduce contact heat loss and improve output performance.

1. Introduction

With the continuous deepening of space exploration and the diversification of exploration tasks, increasing numbers of powerful electronic devices are equipped in spacecrafts [1–5]. These large numbers of electronic devices pose new difficulties and challenges to the spacecraft power supply [6,7]. Worse, in deep space exploration missions, solar cells struggle to produce enough electrical energy for the spacecraft since output power is inversely proportional to the distance from the sun [8,9]. Besides, chemical batteries with stable output cannot power the spacecrafts for the necessary mission times, years if not decades [10,11]. Radioisotope thermoelectric generators (RTGs) have become almost the only power source available in deep space missions due to their long lifetime, high energy density, and high stability [12–14]. RTGs convert the decay heat of radioactive isotopes directly into electrical energy based on the Seebeck effect [15,16]. There are no rotating parts inside the RTGs and no gas is generated, which is a static energy conversion, so maintenance is not required during service [17]. However, the application of RTGs is limited due to the low energy conversion efficiency and related output power. The conversion efficiency can be expressed as $\eta = \frac{T_h - T_c}{T_h} \times \frac{\sqrt{1+Z\overline{T}}-1}{\sqrt{1+Z\overline{T}}+T_c/T_h}$, where T_h and T_c represent the temperature of the hot and cold side of the thermoelectric (TE) legs, respectively; $\overline{T}$ represents the average temperature of the TE legs [18,19], and ZT is the dimensionless figure of merit used to evaluate the TE properties of the materials within the TE legs, which can be expressed as $ZT = \frac{\alpha^2\sigma}{\kappa}T$, where α, σ, and κ denote the Seebeck coefficient, electrical conductivity, and thermal conductivity of the material, respectively; and T is the absolute temperature [20,21]. From the above formulas, to increase the conversion efficiency, not only the ZT needs to be improved, but also the temperature difference between the hot and cold sides of the TE legs should be as large as possible.

The temperature distribution and flow of heat within a TE device are

* Corresponding authors at: Department of Nuclear Science and Technology, Nanjing University of Aeronautics and Astronautics, Nanjing 211106, China.
E-mail addresses: xuzhiheng@nuaa.edu.cn (Z. Xu), tangxiaobin@nuaa.edu.cn (X. Tang).

https://doi.org/10.1016/j.jallcom.2023.173202
Received 20 September 2023; Received in revised form 3 December 2023; Accepted 14 December 2023

Nomenclature

RTG	Radioisotope thermoelectric generator
TE	Thermoelectric
η	Conversion efficiency
T_h	Temperature of the hot side of the thermoelectric leg
T_c	Temperature of the cold side of the thermoelectric leg
$\overline{T}$	Average temperature of the thermoelectric leg
α	Seebeck coefficient
σ	Electrical conductivity
κ	Thermal conductivity
PF	Power factor
ZT_{max}	Maximum ZT value
n	Carrier concentration
μ	Mobility
m^*	Effective mass
k_B	Boltzmann constant
h	Planck constant
e	Electron charge
SPS	Spark plasma sintering
DIW	Direct-ink writing
EC	Ethyl cellulose
Cu	Copper
G'	Storage modulus
G''	Loss modulus
tan δ	Loss tangent
γ	Shear rate
τ	Shear stress
ω	Angular frequency
ΔV	Voltage difference
ΔT	Temperature difference
L	Length
A	Cross-sectional area
R	Resistance
I	Current
U	Voltage
D	Density
C_p	Specific heat capacity
λ	Thermal diffusivity
PCB	Printed circuit board
I-V	Current-voltage
V_{oc}	Open circuit voltage
P_{out}	Output power
P_{max}	Maximum output power
α_p	Seebeck coefficient of p-type thermoelectric material
α_n	Seebeck coefficient of n-type thermoelectric material
N	Number of pairs of thermoelectric legs
R_{in}	Internal resistance
R_L	External resistance
FWHM	Full-width at half of maximum

not only determined by the thermal conductivity of the TE materials, but also by external and architectural factors such as the thermal contacts, heat source/sink conditions, geometry of the TE legs, ambient temperature, wind speed, etc [22,23]. Thus, beyond maximizing the ZT of the TE materials [24,25], among the parameters that can be adjusted to enhance the performance of a TE device, the geometry of the TE legs is a particularly interesting parameter to be optimized. Through theoretical analysis, Sahin et al. proved that the shape parameter can significantly improve the output performance of the TE legs [26]. Besides, Khalil et al. simulated the output performance of TE legs with the same volume but different geometries using the finite element method showing that the highest conversion efficiencies were obtained with Y-shaped legs [27]. Zebin et al. experimentally demonstrated that TE generators with stretchable helical architectures have adjustable temperature differences and improved output power [28]. In a previous work, we proposed two kinds of TE legs with helical and spoke geometries relying on the increment of the side area to enhance heat dissipation [29]. We demonstrated that both the helix- and spoke-shaped TE legs generate higher power than the traditional cylinder- and square-shaped TE legs under natural heat dissipation. Many researchers have demonstrated that the output performance of TE generators can be improved by optimizing the geometry, however, the preparation processes for TE materials with high ZT values, such as hot pressing and spark plasma sintering (SPS), can only fabricate regular shapes such as cylinder and cuboid [30,31]. Thus, many previous attempts to fabricate TE devices with special geometrical shapes to improve output performance or better couple with irregularly shaped heat sources have used 3D printing technologies [29,32,33]. Among 3D printing technologies, direct-ink writing (DIW) 3D printing is most used to fabricate TE materials and devices with arbitrary shapes [34,35]. As an example, Kim et al. fabricated TE half rings by 3D printing using all-inorganic viscoelastic inks to better match the cylindrical heat source [36]. However, inert gas conditions are required for the manufacture of all-inorganic viscoelastic inks, which is a significant constraint for 3D printing. Abu et al. fabricated a trapezoidal-shaped TE prototype using the dispenser printing technique, and demonstrated the special shape to enable the generation of 1.24 times higher voltage and 1.5 times higher power compared to the rectangular-shaped prototype [37]. While 3D printing offers numerous additional degrees of freedom for the design and fabrication of complex shapes, in these previous TE devices fabricated by 3D printing, the TE legs have complex patterns in cross-section, but no complex spatial structure. They are just formed by stretching the complex patterns on the bottom surface along the axis perpendicular to the bottom surface. Thus, there is plenty of room for further optimizing the TE leg geometry using 3D printing technologies and thereby enhancing the output performance of RTGs and TE generators used in other scenarios.

Generally, the printability of a TE slurry and the TE properties of the 3D-printed TE materials are the two most critical factors for DIW 3D printing technology. In terms of printability, the TE slurry needs to have suitable rheological properties, resulting in a smooth extrusion from the needle without clogging and retaining the shape after reaching the substrate. In terms of TE properties, electrical conductivity is the key factor that needs to be improved in slurry-derived TE materials due to the loose contact between TE particles as well as the presence of organic binders.

Herein, we detail our results on the development of a novel TE slurry suitable for 3D printing using organic solvents and binders, which can be synthesized under air conditions. The TE slurry has proper rheological properties so it can be printed into samples with complex spatial structures. Cu powder is added to the TE slurry as a conductive additive. The addition of Cu can improve the crystallinity of TE particles during sintering. Besides, the homogeneous distribution of Cu within the TE materials generates more carriers to increase the electrical conductivity but reduce the Seebeck coefficient to a certain extent. We thoroughly characterize the structural, chemical, and transport properties of the 3D-printed materials, both p- and n-type. Additionally, we demonstrate here their excellent performance by producing TE modules composed of 3D-printed TE legs with unconventional geometries.

2. Materials and method

2.1. TE slurry formulation

A key result of the present work is the formulation of TE slurry

suitable for DIW 3D printing technology under air conditions, i.e., having proper rheological properties and resulting in printed TE legs with excellent TE properties. Ethyl cellulose (EC) with a viscosity of 200 mPa S (>99 %, QASEG) and diethylene glycol monobutyl ether acetate (98 %, Aladdin) were used to synthesize organic binders. Epoxy-resin DER.732 (Sigma-Aldrich) was used as solvent. Commercial bismuth telluride powders (p-type: $Bi_{0.5}Sb_{1.5}Te_3$; n-type: $Bi_2Se_{0.3}Te_{2.7}$, Chengdu Alfa Metal Material Co., Ltd, China) with particle sizes below 10 μm were used as TE filler. Copper (Cu) powder (Chengdu Alfa Metal Material Co., Ltd, China) with particle sizes less than 10 μm was added to the p-type TE slurry as a conductive additive to increase the electrical conductivity. Tween-80 (SCR) as a dispersant was added to the TE slurry to avoid the clustering of copper powders. The above reagents and powders are used directly without further purification.

The schematic of the preparation of the TE slurry is shown in Fig. 1a. DER.732 was used as the solvent with a certain viscosity, and the organic binder was added into the solvent and stirred thoroughly to form the solution with a sufficient viscosity. And the mass ratio of DER.732 to binder is 65:35. Subsequently, TE powder and Cu powder were added to the above solution (sum of DER.732 and binder) in batches during stirring to form TE slurry. Cu powder would cluster in the TE slurry to form larger granules, which can cause the needle blockage. Tween-80 needs to be added to the solution as a dispersant to disperse the Cu powder evenly in the TE slurry. Due to the Schottky barriers generated between the Cu and n-type TE particles that results in an increase of the material electrical resistance, Cu powder was only added to the p-type TE slurry as a conductive additive. After the TE and Cu powders were added to the solution, continuous stirring (usually more than 4 h) was required to make the TE slurry form a uniform colloidal suspension. To achieve the rheological properties suitable for 3D printing, for the n-type slurry, the mass ratio of the solution to the TE powder was 1:9.3. On the other hand, for the p-type slurry, the mass ratio of the solution to the combination of TE and Cu powders was 1:8.8. The percentage of Cu on the total amount of inorganic material was in the range 0–1 %. The difference in the mass ratio of the solution to TE powder comes from the difference in the density of the p-type and n-type TE powders. The mass ratio of Tween-80 to TE slurry (sum of solution, TE and Cu powders) is shown in Table S1 in the Supplementary Materials.

Fig. 1b shows the synthesis schematic and photograph of the organic binder. EC was dissolved in diethylene glycol monobutyl ether acetate to form a gel-like binder, where the mass ratio of EC to the solvent is 1:10. After sintering, there are small amounts of DER.732 and binder present in the 3D-printed samples to increase the hardness and strength, and Cu particles are uniformly distributed in the TE materials as shown in Fig. 1c.

2.2. Fabrication of TE legs using 3D printing

The DIW 3D printer used to fabricate TE legs is shown in Fig. 2a. The TE slurry is loaded into a syringe connected to a high-pressure air circuit to extrude the TE slurry through a needle with a diameter of 260 μm. The shape of the TE leg is defined by the translation of the syringe using an xyz mechanical stage. A computer programmed using G-code controls the displacement of the mechanical stage according to the desired sample shape. The extrusion rate of the TE slurry from the needle is adjusted by the air pressure, which requires comprehensive consideration of the diameter of the needle, the moving speed as well as the rheological properties of the TE slurry. The TE slurry is printed layer-by-layer on a glass substrate to fabricate TE legs with a predefined geometry.

After printing, the samples were dried in an oven at 170 °C for 24 h to evaporate the solution and separate from the substrate. Subsequently,

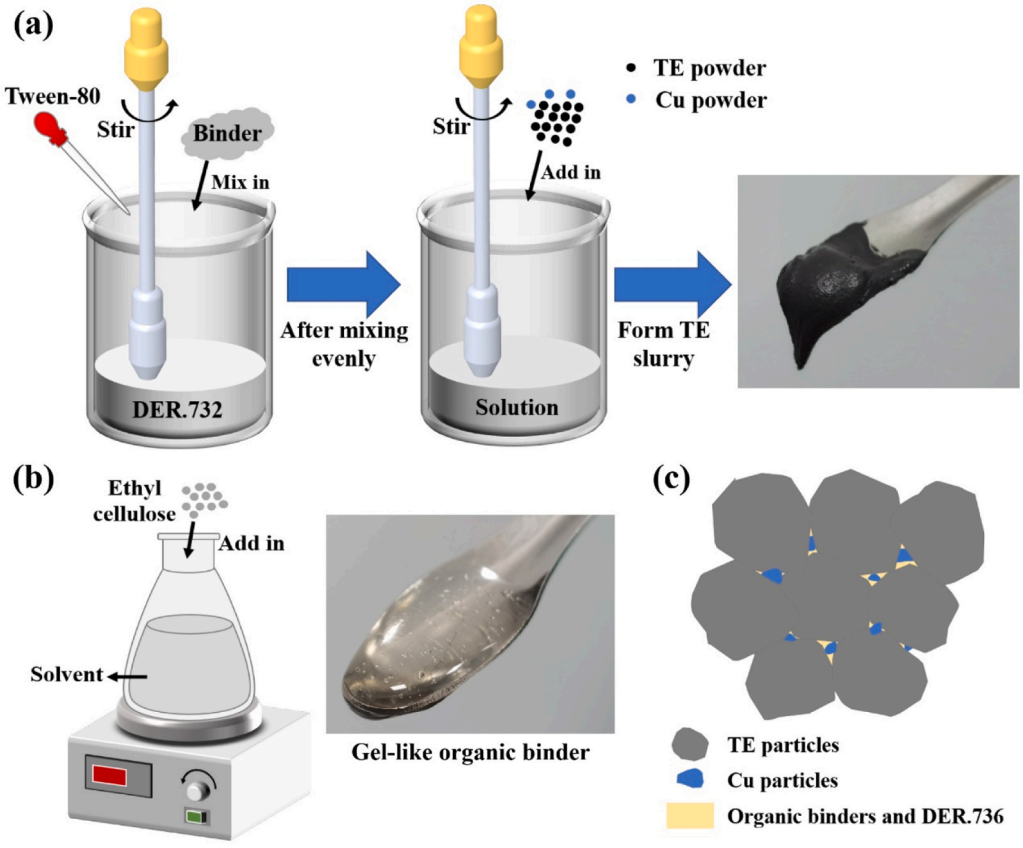

Fig. 1. (a) Schematic diagram of the preparation of the TE slurry; (b) Synthesis schematic and photograph of the organic binder; (c) Schematic illustration of the sintered composite.

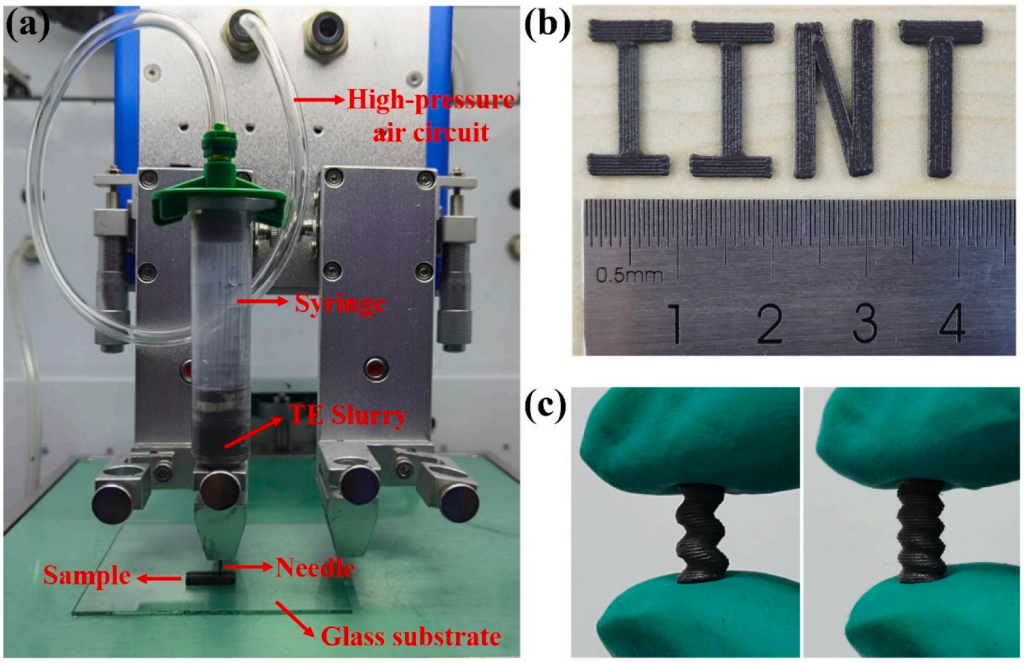

Fig. 2. (a) Molding process of 3D printing; Photographs of (b) letters printed on the substrate and (c) helix-shaped TE legs after drying.

the samples were annealed under N_2 for 6 h to remove the organic binder and sinter the materials. To achieve the best TE properties, the optimal annealing temperature was found to be 450 °C for the p-type and 400 °C for the n-type. Fig. 2b and c show the printed IINT letters and the helix-shaped TE legs after drying, respectively.

2.3. Characterization of slurries and materials

The rheological properties of TE slurries were tested by a rotational rheometer (MCR92) at a temperature of 25 °C. The TE slurry was filled in a gap of 1 mm between two parallel plates, and the rheological properties are determined when applying rotational speed difference between the two plates. The dynamic viscosity and shear stress (τ) were tested in the flow curve mode; the storage modulus (G') and loss modulus (G'') were tested in the amplitude sweep mode with an angular frequency of 10 rad/s; and the loss tangent (tan δ) is tested in the frequency sweep mode, where the tan δ is calculated by the following formulas:

$$\tan\delta = \frac{G''}{G'} \tag{1}$$

where, G' and G'' are the measured storage and loss modulus in the frequency sweep mode, respectively.

The Seebeck coefficient (α), electrical conductivity (σ) and power factor (PF) of the 3D-printed TE materials were measured by the thermoelectric effect system (CTA–3) under a helium atmosphere. They were calculated from the measured data according to the following formulas:

$$\alpha = \frac{\Delta V}{\Delta T} \tag{2}$$

$$\sigma = \frac{L}{RA} \tag{3}$$

$$PF = \alpha^2\sigma \tag{4}$$

where, ΔV and ΔT are the measured voltage difference and temperature difference between the two sides of the sample when one side is heated, respectively; L and A represent the length and cross-sectional area of the sample, respectively; R is the resistance of the sample, which is obtained by Ohm's law: $R = U/I$, where I is the current applied to the sample, and U is the measured voltage across the sample. Carrier concentration (n) and mobility (μ) were obtained by Hall effect test system (HT-50 type) measures at a temperature of 25 °C. The relationship among α, σ and n, μ as follows:

$$\alpha = \frac{8\pi T m^* k_B^2}{3eh^2}\left(\frac{\pi}{3n}\right)^{\frac{2}{3}} \tag{5}$$

$$\sigma = en\mu \tag{6}$$

where, m^* is effective mass, k_B is the Boltzmann constant, h is the Planck constant, e is the electron charge [38]. The thermal conductivity (κ) can be determined from:

$$\kappa = DC_p\lambda \tag{7}$$

where, D is the density of the 3D-printed materials, which is obtained by the Archimedes method; C_p represents the specific heat capacity, which was measured by differential scanning calorimeter (DSC, TA25); λ is the thermal diffusivity, which was measured on the Xenon flash apparatus (XFA 600, Linseis).

2.4. Output performance test of TE modules

Helix-shaped TE legs with geometrical parameters of "$r = 0.25$, $n = 5$" and "$r = 0.5$, $n = 3$" in our previous work were fabricated by 3D printing [29]. The bottom surface of the helix-shaped TE legs is a circle with a radius of 2 mm, and the height of the TE leg is 10 mm. P-type TE slurry with 0.6 % Cu addition content was used to fabricate the p-type TE legs. After sintering, the helix-shaped TE legs were connected into π-shaped single TE modules to test the electrical output characteristics. Customized aluminum printed circuit boards (PCBs) substrate with high electrical and thermal conductivity were used as the electrodes, and the regions not connected to TE legs were coated with electrical insulation to avoid short circuits, as shown in Fig. 3a. Lead-free solder paste ($Sn_{96.5}Ag_{3.0}Cu_{0.5}$) was used to bond the TE legs to the electrodes. Fig. 3b displays the assembled TE modules with helix-shaped TE legs.

The TE modules were placed on the electric heating plate, which surface temperature can be adjusted through resistive heating. The TE

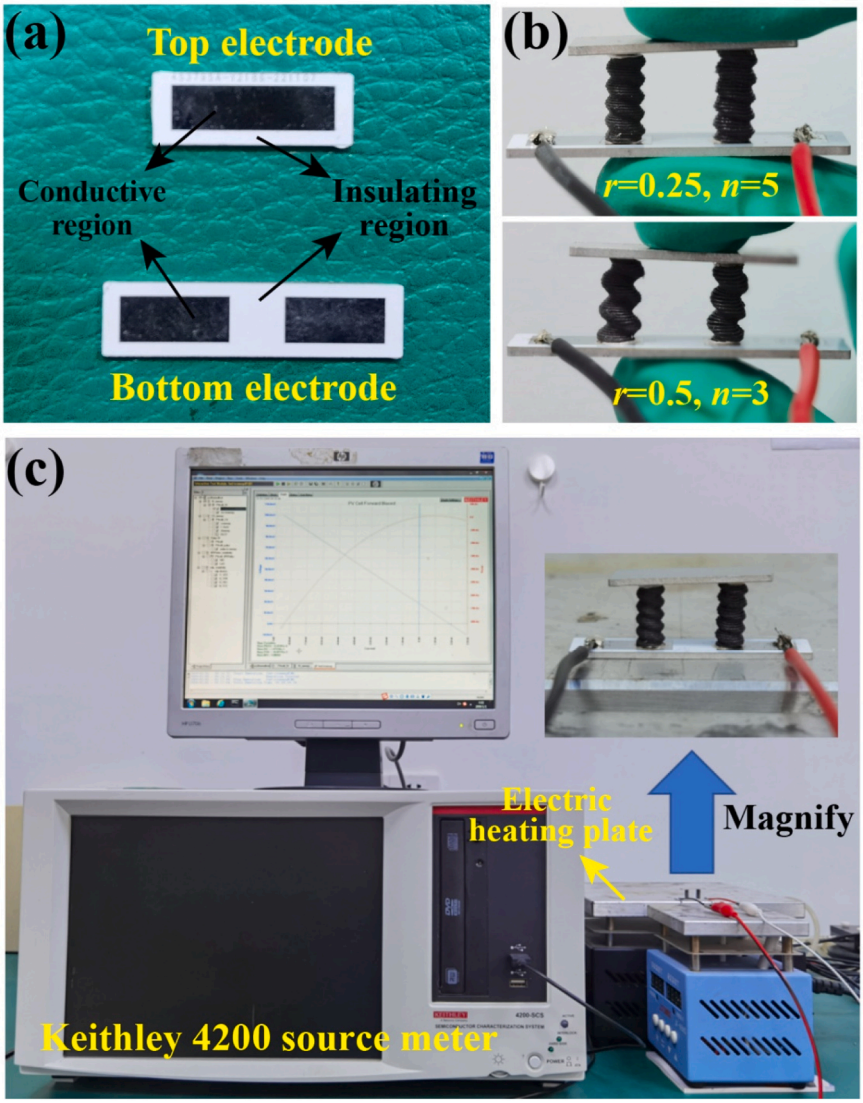

Fig. 3. Photograph of (a) electrodes, (b) helix-shaped TE modules, and (c) electrical output performance measurement system.

modules were in an air environment at a temperature of 293.15 K and naturally dissipates heat into the air. Current-Voltage (*I-V*) characteristic curves of the TE modules were tested by a Keithley 4200 source meter when the temperature is stable for more than 30 min. The open circuit voltage (V_{oc}) and output power (P_{out}) can be calculated by the following formula:

$$V_{oc} = (\alpha_p - \alpha_n)N\Delta T \tag{8}$$

$$P_{out} = \left(\frac{V_{oc}}{R_{in} + R_L}\right)^2 R_L \tag{9}$$

where α_p and α_n are the Seebeck coefficient of the p-type and n-type TE materials, respectively; N is the number of n-type and p-type TE leg pairs, which is 1; ΔT is the temperature difference between the hot and cold sides of the TE legs; R_{in} and R_L are the internal resistance and external resistance of the TE modules, respectively. The P_{out} will reach the maximum output power (P_{max}) when R_{in}=R_L. The measurement system for the TE modules is shown in Fig. 3c. The same TE modules and test conditions as in the experiment were constructed in the finite element analysis software COMSOL to verify the output performance test.

3. Results and discussion

3.1. Rheological properties of thermoelectric slurry

The printability of the TE slurry was evaluated by its rheological properties. The n-type TE slurry and p-type TE slurry with different Cu addition content exhibit the same rheological properties. The rheological properties of the p-type TE slurry without Cu addition are shown in Fig. 4. Fig. 4a shows the variation of dynamic viscosity with shear rate (γ). The dynamic viscosity decreases with the increase of γ, and decreases sharply when γ exceeds 70 1/s, dropping 4 orders of magnitude. This dramatic decrease of the dynamic viscosity with γ is known as shear thinning behavior and allows the TE slurry to be smoothly extruded from fine needles without clogging. The shear stress (τ) of TE slurry as a function of γ is shown in Fig. S1a in the Supplementary Materials. Variations of storage modulus (G') and loss modulus (G'') with shear stress (τ) are shown in Fig. 4b. G' and G'' decrease with increasing τ. While G' is larger than G'' at low $\tau < 20$ Pa, which indicates that TE slurry is in a solid state. As marked by the red arrow in Fig. 4b, when τ exceeds 20 Pa, G' is smaller than the G'', indicating that TE slurry is in the liquid state. At about $\tau = 200$ Pa, G' and G'' increase gradually, which may be due to the change and damage of the internal structure of TE slurry caused by the high temperature generated by the high-speed rotation of the plates

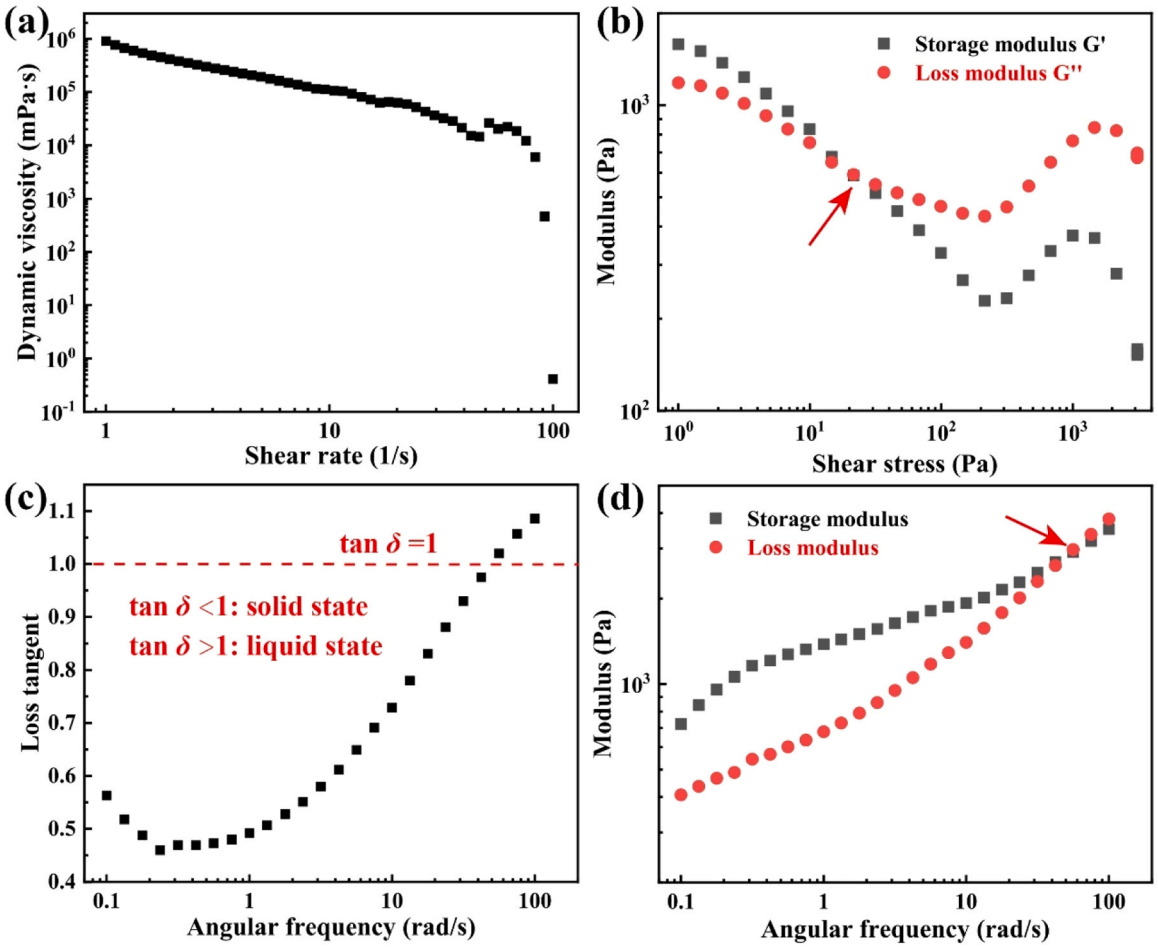

Fig. 4. Rheological properties of TE slurry measured under different test modes. (a) Dynamic viscosity measured under flow curve mode; (b) Storage modulus and loss modulus measured under amplitude sweep mode; (c) Loss tangent, (d) storage modulus and loss modulus measured under frequency sweep mode.

during the test. To ensure a stable printing process, the extrusion rate of the TE slurry should not be too fast, so this situation will not appear in the 3D printing. The loss tangent (tan δ) as a function of angular frequency (ω) is shown in Fig. 4c. As shown by the red dotted line (tan $\delta = 1$), when the ω is less than about 50 rad/s, tan δ is less than 1, which means that the TE slurry is in a solid state; and when the ω exceeds 50 rad/s, the tan δ is greater than 1, which indicates that the TE slurry is in a liquid state. Fig. 4d shows the variation of the G' and G'' with the ω measured in the frequency sweep mode, displaying a magnitude switch in the two modulus as indicated by the red arrow.

The measured rheological properties show that the TE slurry will be smoothly extruded from the needle without clogging. Rheological data also shows that as the applied stress disappears, the TE slurry immediately returns to the initial solid state with high viscosity, the G' greater than G'' and tan $\delta > 1$. Therefore, the TE slurry will not drip from the needle when the air pressure disappeared. What's more, after the TE slurry is extruded from the needle and deposited on the substrate, the printed structure will not collapse or deform. These rheological

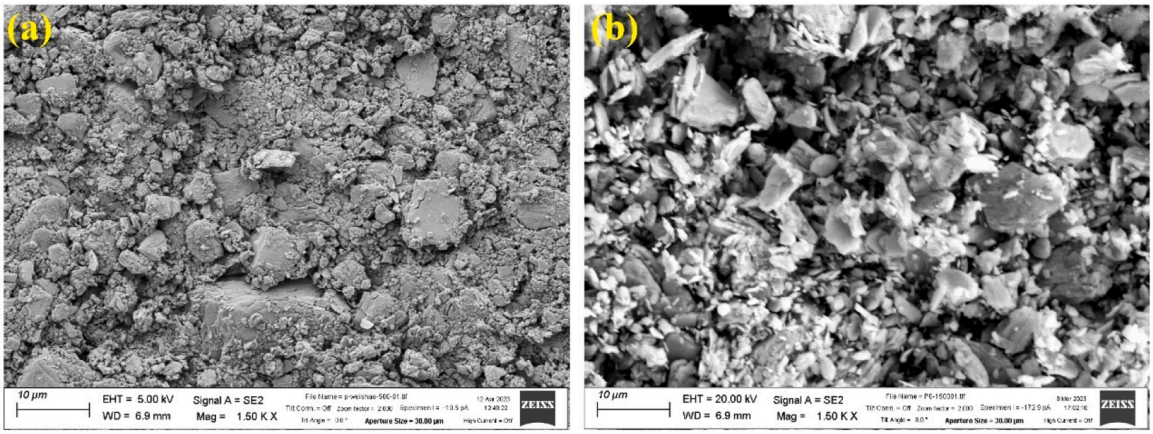

Fig. 5. SEM images of the p-type samples after (a) drying and (b) sintering.

properties enable the TE slurry can be printed into TE legs with spatially complex geometrical shapes.

3.2. Characterization of 3D-printed thermoelectric materials

After the TE slurry is printed into the samples with specific shapes, it needs to be further dried and sintered. Fig. 5 displays SEM images of the p-type samples after drying (before sintering) and after sintering. SEM images of n-type samples are shown in Fig. S2.

As shown in Fig. 5a, TE particles with a broad size distribution co-exist in the 3D-printed samples after drying. Before sintering, TE particles are bound together by the organic binder and thus come in different sizes. After sintering, the organic binder between TE particles and the organic thin film coated on the surface of the TE particles disappeared as shown in Fig. 5b. The material become denser due to the sintering of TE particles.

Fig. 6 displays the SEM image and EDS elemental maps of an n-type sample after sintering. During the printing process, the sample is formed by stacking TE slurry in a layer-by-layer fashion, and no axial pressure acts on the sample. Therefore, the 3D-printed samples have less density compared to the TE materials fabricated by hot pressing and SPS. This can also be reflected in SEM and EDS elemental maps where pores can be observed, as marked by the yellow arrows. According to Archimede' method, the density of the samples was 4.31 g/cm^3.

SEM image and EDS elemental maps of the p-type sample with 0.6 % Cu addition content after sintering are shown in Fig. 7. Some pores can be also observed in the p-type samples as indicated by the yellow arrows. According to Archimede' method, the density of the samples was 4.25 g/cm^3. Cu is evenly distributed in the sample which shows no Cu aggregates (Fig. 7d). According to EDX analysis, the content of Cu in the final material is 1 wt %. SEM images and EDS elemental maps of p-type samples with different Cu addition content after sintering are shown in Figs. S3-S7.

Fig. 8 displays the XRD patterns of the 3D-printed TE materials after sintering. As shown in Fig. 8a, the peak positions in the XRD patterns of the p-type samples with different Cu addition content do not shift, which indicates that Cu does not change the crystal structure and composition of the p-type TE materials during the sintering process. Additionally, no Cu-based secondary phase is observed from the XRD pattern, which indicates that Cu does not react with BiSbTe to generate an additional phase. The Full-width at half of maximum (FWHM) of the XRD patterns first decreases and then increases with the Cu addition content, and reaches the minimum when the Cu addition content is 0.6 %. The decrease in FWHM indicates an improvement in crystallinity. Thus, the proper Cu addition facilitates the crystallization of p-type TE materials during sintering and improves the crystallinity. The XRD pattern of the n-type TE material is shown in Fig. 8b. The patterns of p-type and n-type samples are consistent with single-phase $Bi_{0.5}Sb_{1.5}Te_3$ and $Bi_2Se_{0.3}Te_{2.7}$, respectively. Therefore, it can be concluded that the microstructure and composition of the TE materials are not changed during the printing and sintering processes.

3.3. Thermoelectric properties of 3D-printed materials

The TE properties of the 3D-printed n-type and p-type TE materials with different Cu addition contents are shown in Fig. 9. Fig. 9a shows the variation of the Seebeck coefficient (α) of 3D-printed TE materials with temperature. For the n-type and p-type materials without Cu addition, the α of the p-type decreases with increasing temperature, and the α of the n-type increases first and then decreases with temperature, which is similar to that of bulk materials [39,40]. The addition of Cu significantly reduces the α of the p-type TE materials, but the α decreases slowly with the increase of Cu content. In addition, the α shows an increasing trend with temperature. The reason for the decrease of α may be due to the

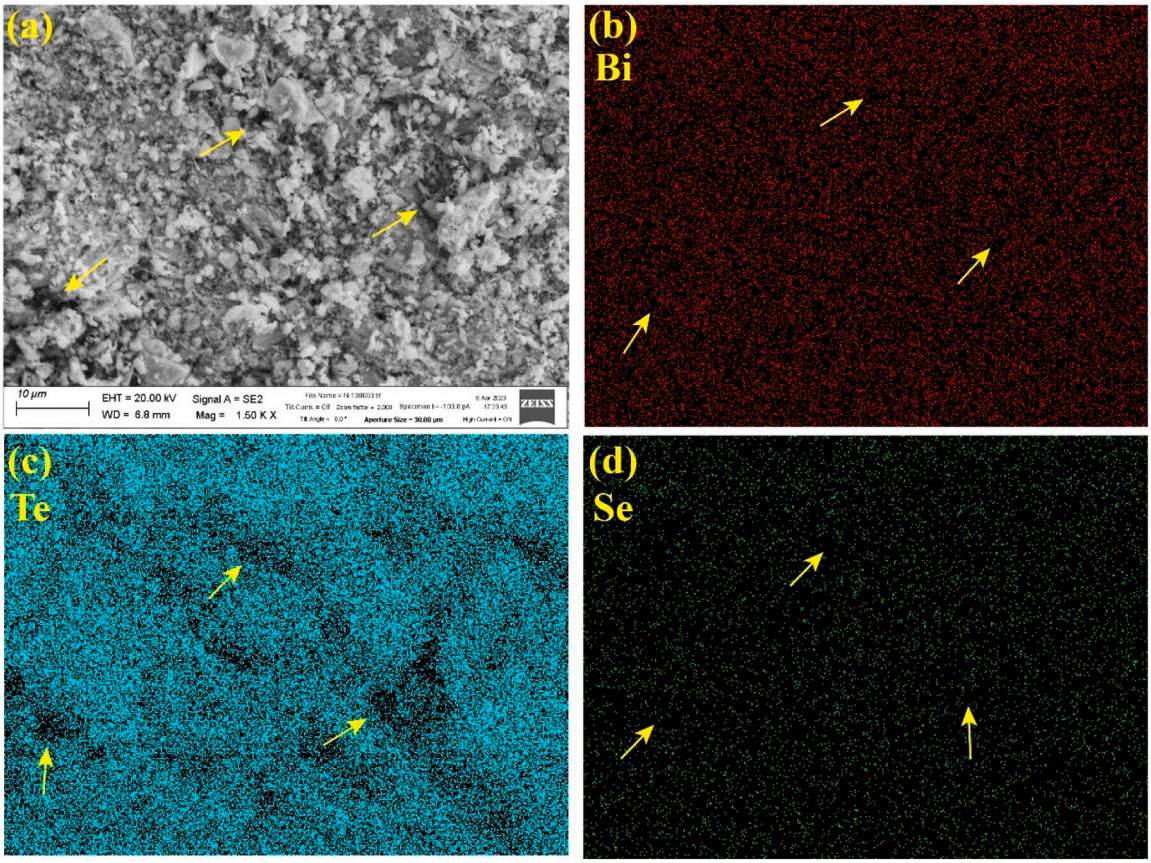

Fig. 6. (a) SEM image and (b-d) EDS elemental maps of n-type samples after sintering.

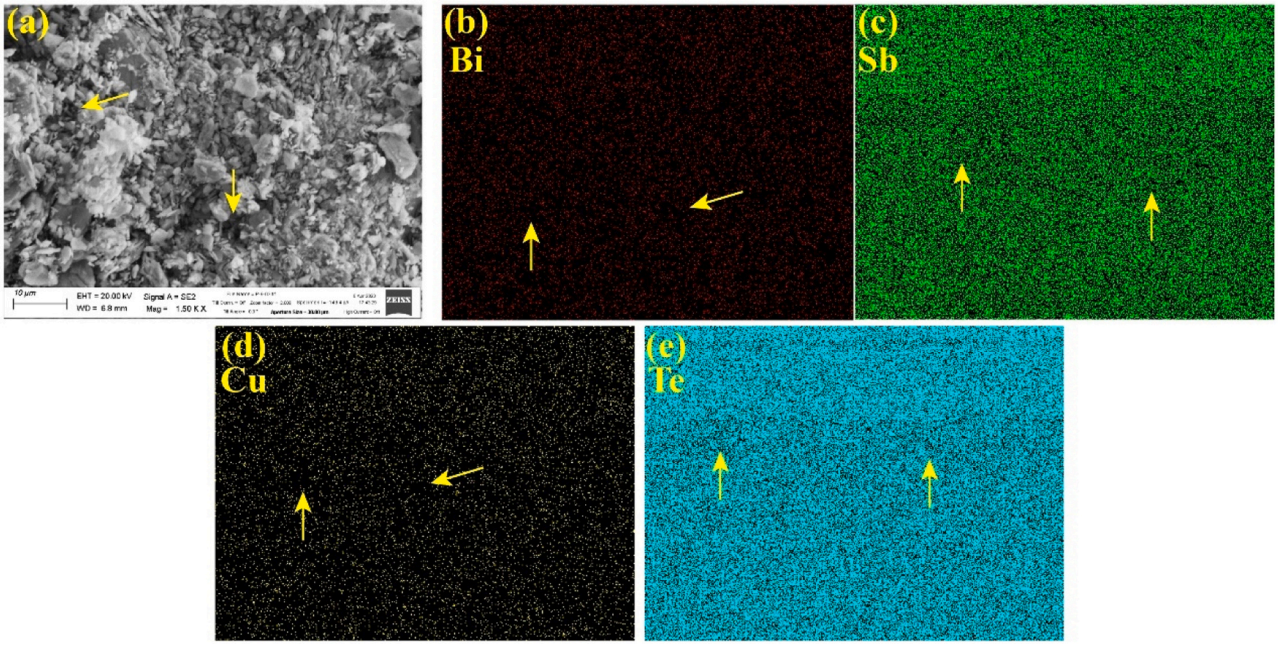

Fig. 7. (a) SEM image and (b-d) EDS elemental maps of the p-type samples with 0.6 % Cu addition content after sintering.

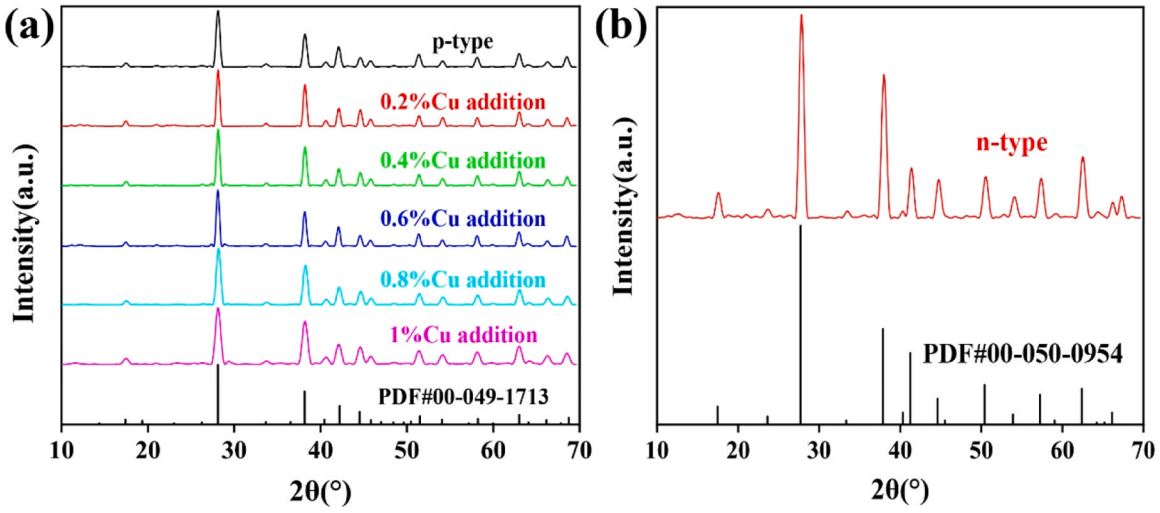

Fig. 8. XRD patterns of 3D-printed TE materials. (a) P-type with different Cu addition content; (b) n-type.

increase in carrier concentration due to the addition of Cu. The electrical conductivity (σ) of the p-type TE materials with Cu addition is significantly higher than that without Cu addition, which proves that Cu acts as a conductive additive within the TE materials. The σ of the p-type increases first and then decreases as the content of Cu increases, and reaches the maximum when the content of Cu is 0.6 % as shown in Fig. 9b. During the preparation of the TE slurry, Tween-80 is added to the TE slurry to prevent the cluster of Cu powder and the amount of Tween-80 is proportional to the content of Cu powder. The added Tween-80 exists in the TE slurry as an organic solution, that is to say, the content of TE and Cu powders in the TE slurry decrease with the addition of Tween-80. Thus, the contact among TE and Cu powders decreases with the addition of Tween-80 and more pores appear in the 3D-printed TE materials after sintering. This is the reason why the σ of the p-type decrease with the increase of the content of Cu when the content exceeds 0.6 %. Considering the effect of Cu on the α and σ, the p-type TE materials with Cu addition exhibit better power factor (*PF*) than that without Cu addition as shown in Fig. 9c.

Carrier concentration (n) and mobility (μ) of the 3D-printed TE materials are shown in Table 1. The n of p-type TE materials with Cu addition is an order of magnitude higher than that without Cu addition. The n increases first and then decreases with the Cu addition content, and reaches the maximum when the content of Cu is 0.6 %. Compared with the p-type material without Cu addition, the increase of n of the p-type material with Cu addition indicates that Cu can inject charge into the TE materials. The large increase in the n leads to an increase in the σ, but a decrease in the α to a certain extent, which can be explained by Formulas. (5) and (6). The decrease of n when the Cu addition content exceeds 0.6 % is associated to the effect of Tween-80. That is, the increasing amounts of Tween-80 introduced reduce at some point the Cu-BST interaction and thus decrease the charge injection effectiveness of the Cu domains. On the other hand, the μ decreases monotonously with Cu addition content due to the increased porosity and potentially to the charge carrier scattering not only at solid-pore but also at the Cu-BST interphases. The addition of Cu changes the behavior of carriers in TE materials, thereby affecting the TE properties.

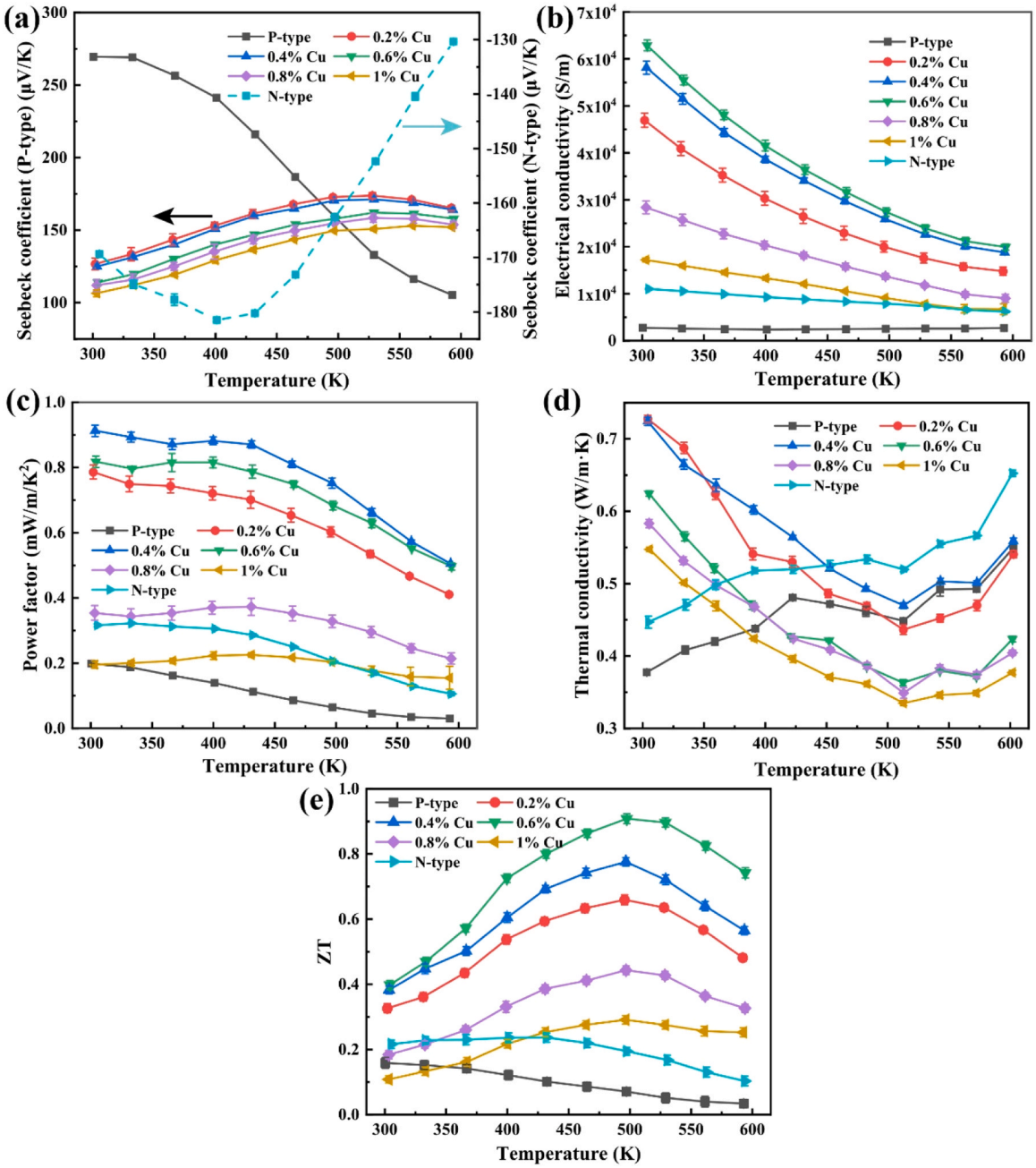

Fig. 9. Thermoelectric properties of 3D-printed thermoelectric composites. (a) Seebeck coefficient; (b) Electrical conductivity; (c) Power factor; (d) Thermal conductivity; (e) ZT value.

Table 1
Carrier concentration and mobility of 3D-printed TE materials.

3D-printed TE materials	Carrier concentration (/cm^3)	Mobility (cm^2/V s)
n-type	2.33E + 19	14.22
p-type	4.85E + 18	21.86
p-type with 0.2 %Cu	2.45E + 19	14.62
p-type with 0.4 %Cu	4.65E + 19	12.85
p-type with 0.6 %Cu	7.38E + 19	11.35
p-type with 0.8 %Cu	6.92E + 19	9.13
p-type with 1 %Cu	5.76E + 19	9.01

Fig. 9d displays the thermal conductivity (κ) of the 3D-printed TE materials. The κ of the n-type and p-type TE materials without Cu addition increase with temperature, which is due to the excitation of minority carriers at high temperatures. From the SEM and XRD results, it can be seen that Cu powder is evenly distributed in the p-type sample, and there is no reaction between Cu and the TE material to produce secondary phases. Therefore, the κ exhibits the superposition of Cu and TE materials, and also exhibits the trend of first increasing and then decreasing with the increase of Cu addition due to the effect of Tween-80.

Based on the above analysis it is clear that ZT increases first and then decreases with the increase of Cu addition as shown in Fig. 9e. The p-type TE material with 0.6 % Cu addition exhibits the best ZT value, and the maximum ZT value (ZT_{max}) is 0.91 at 497 K. The ZT_{max} of the n-type is 0.24 at 432 K. This lower ZT value is related to the lack of suitable conductive additives. The temperature at which ZT_{max} is reached increases with the addition of Cu, which increases the operating temperature range and thus expands the application scenarios of TE devices.

3.4. Output performance of 3D-printed thermoelectric modules

After the helix-shaped TE legs were connected within the TE modules (see details in the Materials and methods section), they were placed on an electric heating plate to test the electrical output performance. The electric heating plate acts as a constant temperature heat source, and the surface temperature is varied from 333.15 K to 393.15 K. The electric heating plate and the TE modules were in the air with a temperature of 293.15 K. The electrical output performances of the helix-shaped TE modules with parameters of "$r = 0.5$, $n = 3$" and "$r = 0.25$, $n = 5$" at different heat source temperatures are shown in Fig. 10.

Fig. 10a shows the open circuit voltage (V_{oc}) of two helix-shaped TE modules as a function of the heat source temperature. The V_{oc} of the two TE modules increases with the heat source temperature as the temperature difference between the hot and cold sides of TE modules increases. For the two TE legs, the helix-shaped TE legs with parameters of "$r = 0.5$, $n = 3$" have a larger side area than the TE legs with parameters of "$r = 0.25$, $n = 5$". Therefore, the helix-shaped TE module with parameters of "$r = 0.5$, $n = 3$" generates larger V_{oc} due to the larger side area for heat dissipation, which increases the temperature difference between the hot and cold sides of the TE module. The helix-shaped TE legs with parameters of "$r = 0.5$, $n = 3$" have a larger resistance due to the extended carrier path, which is proved in our previous work [29]. However, the two TE modules have similar internal resistance due to the greater influence of the contact resistance among TE legs, electrodes and solder paste. The internal resistance and short circuit current of the TE modules as a function of the heat source temperature is shown in Fig. S8.

The helix-shaped TE module with parameters of "$r = 0.5$, $n = 3$" exhibit the larger maximum output power (P_{max}) due to the larger V_{oc} as shown in Fig. 10b. The variation trend of V_{oc} and P_{max} with heat source temperature as well as the comparison of the output performance of the two TE modules in the test results are the same as the simulation results, which indicates that the thermoelectric materials in the two TE modules have the same material properties. What's more, a traditional cuboid-shaped TE module with the same height and volume as the helix-shaped TE modules was fabricated and the photographs are shown in Fig. S9. The comparison of the electrical output performance of the three TE modules is shown in Fig. S10. The two helix-shaped TE modules generate larger V_{oc} and P_{max} than the cuboid-shaped TE module due to the increased side area for heat dissipation, which is consistent with our previous research results [29]. That is, the TE slurry has sufficient uniformity and can print a large number of samples with stable material properties.

I-V characteristic curves of the two helix-shaped TE modules at different heat source temperature are shown in Fig. 10c and d, respectively. Particularly, the helix-shaped TE module with parameters of "$r = 0.5$, $n = 3$" generate a V_{oc} of 38 mV and a P_{max} of 29 μW at a heat source temperature of 393.15 K, which exceeded the 35 mV and 25.5 μW of the helix-shaped TE module with parameters of "$r = 0.25$, $n = 5$". Due to the larger side area for heat dissipation, the helix-shaped TE module with parameters of "$r = 0.5$, $n = 3$" generates the larger temperature difference and V_{oc} than the helix-shaped TE module with parameters of "$r = 0.25$, $n = 5$", and thus generates larger P_{max} because of the similar internal resistance. And the *I-V* characteristic curves of the cuboid-shaped TE module are shown in Fig. S11. The three TE modules exhibit sufficient hardness and strength during the testing, and the variation trend and comparison of output performance in the test results is the same as the simulation results. This shows that the TE slurry has good uniformity and stability, so it can be used to fabricate TE devices with stable output performance and long life.

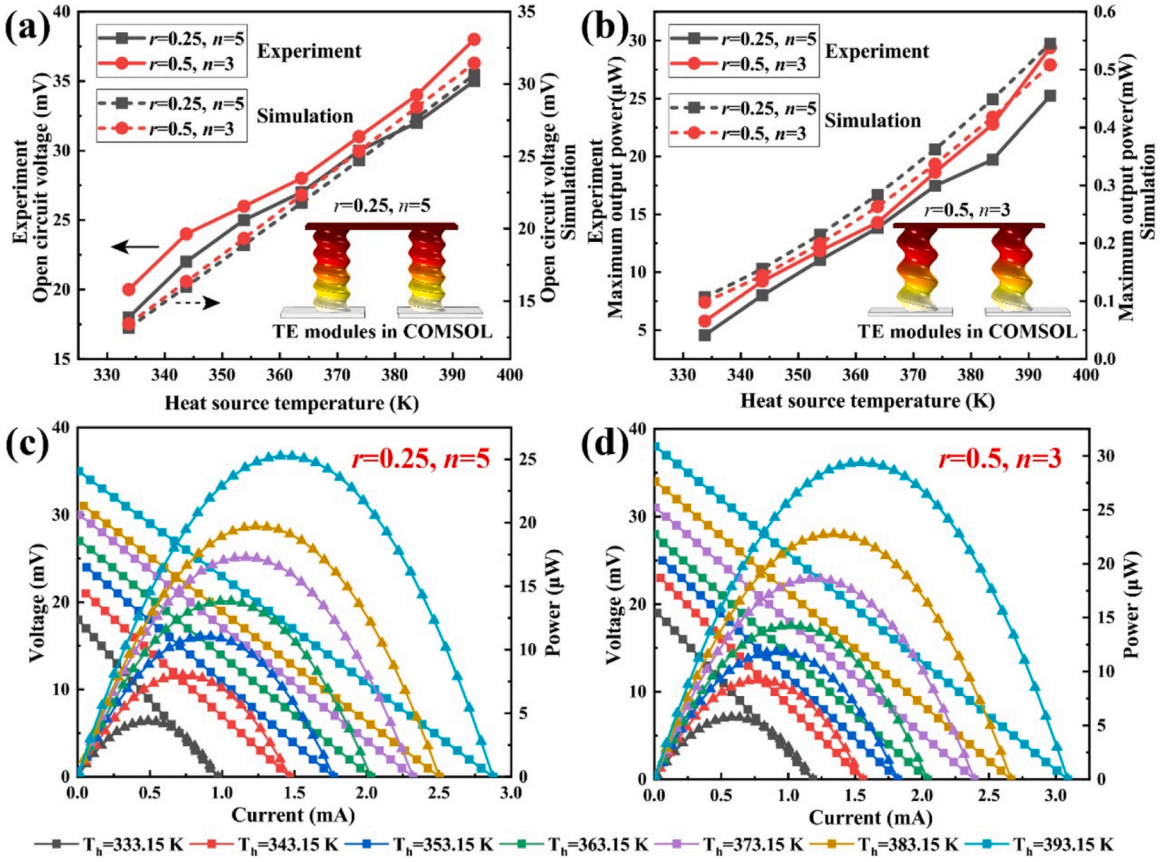

Fig. 10. (a) Open circuit voltage and (b) maximum output power of helix-shaped TE modules under different heat source temperature, and the images of the two TE modules constructed in COMSOL are inserted within them; *I-V* characteristic curves of helix-shaped TE modules with parameters of (c) "$r = 0.25$, $n = 5$" and (d) "$r = 0.5$, $n = 3$".

4. Conclusion

To improve the output performance of TE generators, we developed a novel TE slurry based on organic binders and solvents to fabricate TE legs with special geometrical shapes using 3D printing technology. The proper ratio of organic solvent, binder and TE powder enables TE slurry with suitable rheological properties, which can be smoothly extruded from the needle without clogging, and result in printed samples that maintain specific shapes without collapsing. Cu powder is added to the p-type TE slurry as a conductive additive. Cu is homogeneously distributed within the 3D-printed materials, it does not react with BiSbTe to generate additional phases, but it facilitates the sintering of the TE material. The addition of Cu significantly increases electrical conductivity and improves *ZT*, although it reduces the Seebeck coefficient to some extent. At the same time, the addition of Cu increases the optimum temperature range of operation, which may increase the application scenarios of TE devices. The 3D-printed TE materials exhibit maximum *ZT* values of 0.91 for p-type ($Bi_{0.5}Sb_{1.5}Te_3$) and 0.24 for n-type ($Bi_2Se_{0.3}Te_{2.7}$). The helix-shaped TE modules composed of 3D-printed legs show excellent output performance and structural strength, and the comparison of test results matches the simulation, which proves the uniformity of the TE slurry and the stability of the 3D-printed TE materials. This novel TE slurry can also be used to fabricate other TE devices with special geometrical shapes to match irregularly shaped heat sources to reduce contact heat loss and improve output performance.

CRediT authorship contribution statement

Mingxin Bian: Conceptualization, Data curation, Investigation, Methodology, Validation, Writing – original draft. **Zhiheng Xu:** Data curation, Formal analysis, Investigation, Methodology, Writing – review & editing. **Xiaobin Tang:** Conceptualization, Funding acquisition, Investigation, Writing – review & editing. **Hongyang Jia:** Conceptualization, Formal analysis, Supervision, Writing – review & editing. **Yuqiao Wang:** Data curation, Funding acquisition, Project administration, Validation, Writing – review & editing. **Andreu Cabot:** Funding acquisition, Investigation, Resources, Supervision, Writing – review & editing.

Declaration of Competing Interest

The authors declare that they have no known competing financial interests or personal relationships that could have appeared to influence the work reported in this paper.

Data availability

Data will be made available on request.

Acknowledgments

We thank Prof. Kelum Gamage of the University of Glasgow for his careful revision and improvement of this paper. This work was supported by the National Natural Science Foundation of China (Grant No. 12275132), the Shanghai Aerospace Science and Technology Innovation Foundation (Grant No. SAST2020-097), the Ministry of Science and Technology Foreign Expert Project (Grant No. G2022181007L), and the Postdoctoral Research Foundation of China (2022M711613). We thank the Large-scale Instrument and Equipment Sharing Fund of Nanjing University of Aeronautics and Astronautics for funding.

Appendix A. Supporting information

Supplementary data associated with this article can be found in the online version at doi:10.1016/j.jallcom.2023.173202.

References

[1] M. Howell, V. Kodali, R. Segall, H. Aboudja, D. Berleant, Moore's law and space exploration: new insights and next steps, J. Ark. Acad. Sci. 73 (2019) 13–17, https://doi.org/10.54119/jaas.2019.7303.
[2] E. Afshinnekoo, R.T. Scott, M.J. MacKay, E. Pariset, E. Cekanaviciute, R. Barker, S. Gilroy, D. Hassane, S.M. Smith, S.R. Zwart, Fundamental biological features of spaceflight: advancing the field to enable deep-space exploration, Cell 183 (2020) 1162–1184, https://doi.org/10.1016/j.cell.2020.10.050.
[3] W. Wu, W. Liu, D. Qiao, D. Jie, Investigation on the development of deep space exploration, Sci. China Technol. Sci. 55 (2012) 1086–1091, https://doi.org/10.1007/s11431-012-4759-z.
[4] K. Schilling, Perspectives for miniaturized, distributed, networked cooperating systems for space exploration, Rob. Auton. Syst. 90 (2017) 118–124, https://doi.org/10.1016/j.robot.2016.10.007.
[5] E. Turan, S. Speretta, E. Gill, Autonomous navigation for deep space small satellites: scientific and technological advances, Acta Astronaut (2022), https://doi.org/10.1016/j.actaastro.2021.12.030.
[6] I. Levchenko, K. Bazaka, T. Belmonte, M. Keidar, S. Xu, Advanced materials for next-generation spacecraft, Adv. Mater. 30 (2018), 1802201, https://doi.org/10.1002/adma.201802201.
[7] S.H. Yeo, H. Ogawa, D. Kahnfeld, R. Schneider, Miniaturization perspectives of electrostatic propulsion for small spacecraft platforms, Prog. Aerosp. Sci. 126 (2021), 100742, https://doi.org/10.1016/j.paerosci.2021.100742.
[8] A.W.Y. Ho-Baillie, H.G.J. Sullivan, T.A. Bannerman, H.P. Talathi, J. Bing, S. Tang, A. Xu, D. Bhattacharyya, I.H. Cairns, D.R. McKenzie, Deployment opportunities for space photovoltaics and the prospects for perovskite solar cells, Adv. Mater. Technol. 7 (2022), 2101059, https://doi.org/10.1002/admt.202101059.
[9] J.M. Raya-Armenta, N. Bazmohammadi, J.C. Vasquez, J.M. Guerrero, A short review of radiation-induced degradation of III-V photovoltaic cells for space applications, Sol. Energy Mater. Sol. Cells 233 (2021), 111379, https://doi.org/10.1016/j.solmat.2021.111379.
[10] A. Fly, I. Kirkpatrick, R. Chen, Low temperature performance evaluation of electrochemical energy storage technologies, Appl. Therm. Eng. 189 (2021), 116750, https://doi.org/10.1016/j.applthermaleng.2021.116750.
[11] A.D. Pathak, S. Saha, V.K. Bharti, M.M. Gaikwad, C.S. Sharma, A review on battery technology for space application, J. Energy Storage 61 (2023), 106792, https://doi.org/10.1016/j.est.2023.106792.
[12] K. Liu, X. Tang, Y. Liu, Z. Xu, Z. Yuan, J. Li, Z. Zhang, Preparation and optimization of miniaturized radioisotope thermoelectric generator based on concentric filament architecture, J. Power Sources 407 (2018) 14–22, https://doi.org/10.1016/j.jpowsour.2018.10.052.
[13] Q. Tan, W. Sun, Z. Li, J.-F. Li, Enhanced thermoelectric properties of earth-abundant Cu_2SnS_3 via In doping effect, J. Alloy. Compd. 672 (2016) 558–563, https://doi.org/10.1016/j.jallcom.2016.02.185.
[14] Y. Liu, Y. Zhang, Q. Xiang, F. Hao, Q. An, H. Chen, Comprehensive modeling and parametric analysis of multi-mission radioisotope thermoelectric generator, Appl. Therm. Eng. 219 (2023), 119447, https://doi.org/10.1016/j.applthermaleng.2022.119447.
[15] K. Liu, X. Tang, Y. Liu, Z. Xu, Z. Yuan, Z. Zhang, Enhancing the performance of fully-scaled structure-adjustable 3D thermoelectric devices based on cold-press sintering and molding, Energy 206 (2020), 118096, https://doi.org/10.1016/j.energy.2020.118096.
[16] K. Liu, Y. Liu, Z. Xu, Z. Zhang, Z. Yuan, X. Guo, Z. Jin, X. Tang, Experimental prototype and simulation optimization of micro-radial milliwatt-power radioisotope thermoelectric generator, Appl. Therm. Eng. 125 (2017) 425–431, https://doi.org/10.1016/j.applthermaleng.2017.07.022.
[17] M. Prelas, M. Boraas, F.D.L.T. Aguilar, J.-D. Seelig, M.T. Tchouaso, D. Wisniewski, Nuclear Batteries and Radioisotopes, Springer, 2016.
[18] F. Tohidi, S.G. Holagh, A. Chitsaz, Thermoelectric generators: a comprehensive review of characteristics and applications, Appl. Therm. Eng. 201 (2022), 117793, https://doi.org/10.1016/j.applthermaleng.2021.117793.
[19] S. Ortega, M. Ibáñez, Y. Liu, Y. Zhang, M.V. Kovalenko, D. Cadavid, A. Cabot, Bottom-up engineering of thermoelectric nanomaterials and devices from solution-processed nanoparticle building blocks, Chem. Soc. Rev. 46 (2017) 3510–3528, https://doi.org/10.1039/C6CS00567E.
[20] G.J. Snyder, A.H. Snyder, Figure of merit ZT of a thermoelectric device defined from materials properties, Energy Environ. Sci. 10 (2017) 2280–2283, https://doi.org/10.1039/C7EE02007D.
[21] B. Cai, H. Hu, H.-L. Zhuang, J.-F. Li, Promising materials for thermoelectric applications, J. Alloy. Compd. 806 (2019) 471–486, https://doi.org/10.1016/j.jallcom.2019.07.147.
[22] F. Tohidi, S.G. Holagh, A. Chitsaz, Thermoelectric generators: a comprehensive review of characteristics and applications, Appl. Therm. Eng. 201 (2022), 117793, https://doi.org/10.1016/j.applthermaleng.2021.117793.
[23] S. Khan, T.A. Cheema, A. Abbas, R. Ullah, C.W. Park, Impact of environmental factors on night-time electricity generation using thermoelectric generator, Sustain. Energy Technol. Assess. 56 (2023), 103000, https://doi.org/10.1016/j.seta.2022.103000.
[24] C. Xing, Y. Zhang, K. Xiao, X. Han, Y. Liu, B. Nan, M.G. Ramon, K.H. Lim, J. Li, J. Arbiol, Thermoelectric performance of surface-engineered $Cu_{1.5-x}Te$-Cu_2Se nanocomposites, ACS Nano (2023).
[25] B. Nan, X. Song, C. Chang, K. Xiao, Y. Zhang, L. Yang, S. Horta, J. Li, K.H. Lim, M. Ibáñez, Bottom-up synthesis of SnTe-based thermoelectric composites, ACS Appl. Mater. Interfaces (2023), https://doi.org/10.1021/acsami.3c00625.

[26] A.Z. Sahin, B.S. Yilbas, The thermoelement as thermoelectric power generator: effect of leg geometry on the efficiency and power generation, Energy Convers. Manag. 65 (2013) 26–32, https://doi.org/10.1016/j.enconman.2012.07.020.
[27] Al Khalil, A. Elhassnaoui, S. Yadir, O. Abdellatif, Y. Errami, S. Sahnoun, Performance comparison of TEGs for diverse variable leg geometry with the same leg volume, Energy 224 (2021), 119967, https://doi.org/10.1016/j.energy.2021.119967.
[28] J.P. Rojas, D. Singh, D. Conchouso, A. Arevalo, I.G. Foulds, M.M. Hussain, Stretchable helical architecture inorganic-organic hetero thermoelectric generator, Nano Energy 30 (2016) 691–699, https://doi.org/10.1016/j.nanoen.2016.10.054.
[29] M. Bian, Z. Xu, C. Meng, H. Zhao, X. Tang, Novel geometric design of thermoelectric leg based on 3D printing for radioisotope thermoelectric generator, Appl. Therm. Eng. 212 (2022), 118514, https://doi.org/10.1016/j.applthermaleng.2022.118514.
[30] S. Singh, J. Alemzadeh, G. Rodriguez, M. Phillips, D. Zabek, M. Burton, V.G. Rocha, G. Min, Thermoelectric Properties of Fe-Cr-Ti-Al Synthesised by Mechanical Alloying and Spark Plasma Sintering, Available SSRN 4200048. (n.d.), ⟨https://doi.org/10.2139/ssrn.4200048⟩.
[31] D. Zhang, J. Lei, W. Guan, Z. Ma, C. Wang, L. Zhang, Z. Cheng, Y. Wang, Enhanced thermoelectric performance of BiSbTe alloy: energy filtering effect of nanoprecipitates and the effect of SiC nanoparticles, J. Alloy. Compd. 784 (2019) 1276–1283, https://doi.org/10.1016/j.jallcom.2019.01.084.
[32] J. Lee, S. Choo, H. Ju, J. Hong, S.E. Yang, F. Kim, D.H. Gu, J. Jang, G. Kim, S. Ahn, Doping-induced viscoelasticity in PbTe thermoelectric inks for 3D printing of power-generating tubes, Adv. Energy Mater. 11 (2021), 2100190, https://doi.org/10.1002/aenm.202100190.
[33] N. Su, P. Zhu, Y. Pan, F. Li, B. Li, 3D-printing of shape-controllable thermoelectric devices with enhanced output performance, Energy 195 (2020), 116892, https://doi.org/10.1016/j.energy.2019.116892.
[34] Z. Wang, W. Cui, H. Yuan, X. Kang, Z. Zheng, W. Qiu, Q. Hu, J. Tang, X. Cui, Direct ink writing of Bi_2Te_3-based thermoelectric materials induced by rheological design, Mater. Today Energy 31 (2023), 101206, https://doi.org/10.1016/j.mtener.2022.101206.
[35] S.E. Yang, F. Kim, F. Ejaz, G.S. Lee, H. Ju, S. Choo, J. Lee, G. Kim, S. Jung, S. Ahn, Composition-segmented BiSbTe thermoelectric generator fabricated by multimaterial 3D printing, Nano Energy 81 (2021), 105638, https://doi.org/10.1016/j.nanoen.2020.105638.
[36] F. Kim, B. Kwon, Y. Eom, J.E. Lee, S. Park, S. Jo, S.H. Park, B.-S. Kim, H.J. Im, M. H. Lee, 3D printing of shape-conformable thermoelectric materials using all-inorganic Bi_2Te_3-based inks, Nat. Energy 3 (2018) 301–309, https://doi.org/10.1038/s41560-017-0071-2.
[37] A.R.M. Siddique, S. Mahmud, B. Van Heyst, Performance comparison between rectangular and trapezoidal-shaped thermoelectric legs manufactured by a dispenser printing technique, Energy 196 (2020), 117089, https://doi.org/10.1016/j.energy.2020.117089.
[38] S. Wang, Y. Xiao, D. Ren, L. Su, Y. Qiu, L.-D. Zhao, Enhancing thermoelectric performance of BiSbSe3 through improving carrier mobility via percolating carrier transports, J. Alloy. Compd. 836 (2020), 155473, https://doi.org/10.1016/j.jallcom.2020.155473.
[39] Y. Pan, T.-R. Wei, Q. Cao, J.-F. Li, Mechanically enhanced p-and n-type Bi_2Te_3-based thermoelectric materials reprocessed from commercial ingots by ball milling and spark plasma sintering, Mater. Sci. Eng. B. 197 (2015) 75–81, https://doi.org/10.1016/j.mseb.2015.03.011.
[40] I.T. Witting, T.C. Chasapis, F. Ricci, M. Peters, N.A. Heinz, G. Hautier, G.J. Snyder, The thermoelectric properties of bismuth telluride, Adv. Electron. Mater. 5 (2019), 1800904, https://doi.org/10.1002/aelm.201800904.